Available at
www.ElsevierComputerScience.com
POWERED BY SCIENCE DIRECT®

Signal Processing 84 (2004) 743–762

SIGNAL PROCESSING

www.elsevier.com/locate/sigpro

Modeling anisotropic undersampling of magnetic resonance angiographies and reconstruction of a high-resolution isotropic volume using half-quadratic regularization techniques

Elodie Roullot[a,b,1], Alain Herment[b], Isabelle Bloch[a,*], Alain de Cesare[b], Mila Nikolova[a], Elie Mousseaux[b,c]

[a] *Département TSI-CNRS UMR 5141 LTCI, Ecole Nationale Supérieure des Télécommunications, 46 rue Barrault, 75013 Paris, France*
[b] *INSERM U494, Paris, France*
[c] *Hopital Européen Georges Pompidou (HEGP), Paris, France*

Received 28 July 2003

Abstract

In this paper we address the problem of reconstructing a high resolution volumic image from several low resolution data sets. A solution to this problem is proposed in the particular framework of magnetic resonance angiography (MRA), where the resolution is limited by a trade-off between the spatial resolution and the acquisition time, both being proportional to the number of samples acquired in k-space. For this purpose only the meaningful spatial frequencies of the 3D k-space of the vessel are acquired, which is achieved using successive acquisitions with decreased spatial resolution, leading to highly anisotropic data sets in one or two specific directions. The reconstruction of the MRA volume from these data sets relies on an edge-preserving regularization method and leads to two different implementations: the first one is based on a conjugate gradient algorithm, and the second one on half-quadratic developments. The hyper parameters of the method were experimentally determined using a set of simulated data, and promising results were obtained on aorta and carotid artery acquisitions, where on the one hand a good fidelity to the acquired data is maintained, and on the other hand homogeneous areas are smooth and edges are well preserved. Half-quadratic regularization proved to be particularly well adapted to the MRA problem and leads to a fast iterative algorithm requiring only scalar and FFT computations.

Keywords: Magnetic resonance angiography; High-resolution; Undersampling; Edge-preserving regularization; Half-quadratic regularization

1. Introduction

Due to its numerous advantages for the patient (non-allergenic, non-ionizing), magnetic resonance angiography (MRA) already challenges X-ray Angiography as the reference modality for the imaging of the large arteries and peripheral vascular network

* Corresponding author. Tel.: +33-1-45-817585; fax: +33-1-45-813794.
E-mail addresses: roullot@esme.fr (E. Roullot), alain.herment@imed.jussieu.fr (A. Herment), isabelle.bloch@enst.fr (I. Bloch), decesare@imed.jussieu.fr (A. de Cesare), mila.nikolova@enst.fr (M. Nikolova), elie.mousseaux@egp.ap-hop-paris.fr (E. Mousseaux).
[1] Current address: ESME-Sudria, 4 rue Blaise Desgoffe, 75006 Paris, France.

0165-1684/$ - see front matter © 2003 Elsevier B.V. All rights reserved.
doi:10.1016/j.sigpro.2003.12.013

[26]. Magnetic resonance imaging (MRI) relies on the so-called "frequency (respectively phase) encoding" principle: the frequencies (respectively the phases) of the received signals are proportional to the spatial positions of the voxels which emitted those signals, provided that convenient magnetic gradient fields have been applied during the acquisition. As a consequence, the data acquired in MRI are the Fourier transform of the image and are called "k-space".

When acquiring a 3D MR volume, spatial discrimination is achieved using frequency encoding in one direction and phase encoding in the two other directions. The acquisition time of a 3D MRA data set is

$$T_{\mathrm{acq}} = T_{\mathrm{R}} N_{\phi} N_{\Phi}, \tag{1}$$

where the repetition time T_{R} includes the time needed to measure a "line" of the k-space along the frequency encoding direction, and N_{ϕ} and N_{Φ} are the numbers of encoding steps in both phase encoding directions. The voxel size can be expressed as

$$V = k \frac{1}{N_{\phi}} \frac{1}{N_{\Phi}}, \tag{2}$$

where k is a constant depending on the acquisition setup.

Eqs. (1) and (2) show that 3D MRI is drastically limited by a trade-off between the acquisition time and the spatial resolution.

In order to reduce the acquisition time, technical improvements have been implemented such as the development of very fast and intense space encoding gradients.

Acquiring larger and larger regions of the k-space with a single RF pulse has also been proposed. This approach leads to multishot or EPI sequences, most often designed for Cartesian k-space, but also leads to the development of non-Cartesian k-space fillings. Time-sparing k-space trajectories are, for example, spiral trajectories [11], circular sampling [3,30], rosette trajectories [21], or PROPELLER line trajectories [23]. These data have to be converted to a Cartesian grid before to be transformed into the MR image; this resampling is achieved using interpolation methods [22] or, most often, gridding methods [29].

Acquiring an incomplete k-space was proposed as an alternative to the previously mentioned techniques and was mainly implemented using Cartesian grid acquisitions. The simplest way to spare time during the acquisition is to omit a number of lines. Half-k-space techniques omit almost all "positive" frequencies in a given phase encoding direction except in the center of the k-space, and use the symmetry properties of the Fourier transform of real data to estimate the missing "half-k-space". Cao et al. [7] as well as Plevritis et al. [24] use anatomical prior knowledge to optimally choose the samples to omit. Dologlou et al. [12] present an SVD-based estimation of these missing samples.

We propose a different approach to improve acquisition time without degrading the resolution, consisting in acquiring only the k-space regions containing the useful spatial frequencies of the gadolinium enhanced vessel [18]. It was shown that using two or three double oblique acquisitions orthogonal to each other made it possible to collect the k-space data adapted to reconstruct a stenosed artery segment in routine examinations. The method, unlike previous ones, does not try to cover the whole k-space. The previously mentioned methods achieve a time gain using a sparse sampling of the k-space, but they keep trying to cover both the low and high frequencies of the k-space. Here a dense sampling is proposed, but for each acquisition a selection is made to only acquire the meaningful frequencies, which is also a way to decrease the acquisition time.

In practice, the method can be formulated in the image domain as the acquisition of few volumic data sets with complementary resolutions, each of them containing the high frequencies missing in the other ones. Then the reconstruction of a unique high-resolution isotropic volume is performed.

This paper investigates the possibility to significantly improve the quality of the MRA reconstruction by introducing edge-preserving regularization techniques.

Because the center of k-space is favored by the acquisition process, the frequency content of the white homogenous gadolinium enhanced vessels may be correctly accounted for. In addition we introduced a L2 norm regularization term to further improve homogeneity and SNR of the vascular image. Concerning the edges of the vessel, it is expected that the high frequencies missing in one acquisition will be substituted by the high frequencies contained in the other acquisitions. However, sharp and precisely located edges being a major requirement for

segmentation and quantization of vessels in MRA, we also introduce some a priori knowledge into the reconstruction method in order to further outline edges. This is achieved by using edge-preserving regularization techniques. Finally we expect that edge restoration will also contribute to improve the quality of the reconstruction when the vessel is incorrectly aligned in the geometry of the k-space acquisition. In this case, some additional high frequencies can be missed because the frequency support of the image is no more totally included in the acquired k-space.

Section 2.1 presents the original acquisition sequence on which our work is based, whereas Section 2.2 describes the reconstruction method. In order to solve the combination problem, an accurate modeling of the anisotropic undersampling of M.R. images is required, which is presented in Section 3.1. The criteria for combining the acquisitions are expressed as an energy function to be minimized, detailed in Section 3.2. In Section 4 we show how to take advantage of both the properties of the model in the spectral domain, and those of half-quadratic regularization algorithms, leading to the development of a simple and efficient reconstruction algorithm. Results were validated on simulated data (Section 5) and results on real data are shown in Section 6.

2. Acquisition and combination strategy

2.1. Description of the acquisition process

In this section, we present the acquisition scheme, which consists in acquiring three anisotropically undersampled 3D MR volumes.

Since the acquisition time is proportional to the image dimensions in both phase encoding directions for an unchanged field of view (i.e. an unchanged value of the product *voxel dimension* × *number of voxels*) in each direction of the space, the acquisition time can thus be reduced by decreasing the number of voxels in both phase encoding directions.

Accordingly, we propose to acquire three volumes, each having decreased resolutions along both phase encoding directions. This is achieved by permutation of the frequency encoding direction, so that for each direction, at least one of the three volumes presents a "good" resolution (Fig. 1b). The so-called "reference volume" of Fig. 1a is the volume that would be acquired in a conventional acquisition scheme providing in each direction the best of the resolutions of the three volumes in the considered direction. An isotropic reference volume is dealt with in the following for the sake of readability.

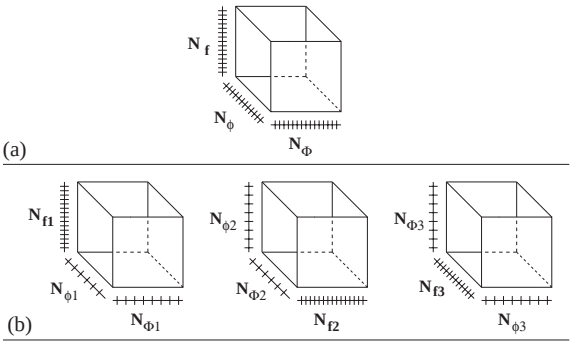

Fig. 1. (a) The reference volume, obtained with a conventional acquisition scheme. (b) The acquisition strategy in the general case, which consists in decreasing the resolution in both phase encoding directions for each acquisition, and in permutating the encoding directions between the different acquisitions.

According to the properties of the Fourier transform, acquiring an undersampled volume corresponds to acquiring a truncated k-space, i.e. a k-space without the highest frequencies along the undersampling direction.

It would also be possible to acquire two volumes instead of three, and thus to decrease the resolution in only one of the two phase encoding directions, in order to always keep two "good" resolutions in any of the volumes for each direction. In the following, for the sake of generality we will always consider the three-acquisition case in our theoretical developments.

Having defined the acquisition sequence, we can now compute the resulting acquisition time according to Eq. (1). Let N_{fi} be the numbers of voxels in the frequency encoding direction in the ith volume, and $N_{\Phi i}$ and $N_{\phi i}$ the numbers of voxels in both phase encoding directions, according to Fig. 1. The repetition time T_R is supposed to be the same for all the acquisitions. Let us recall that a variable number of voxels in the frequency direction would not lead to any improvement, since it does not affect significantly the acquisition time.

According to Eq. (1), the time needed to acquire the ith volume V_i (i varying from 1 to 3) is

$$T_i = T_R N_{\Phi i} N_{\phi i} \tag{3}$$

leading to a total acquisition time of

$$T_{1+2+3} = T_R(N_{\phi 1}N_{\Phi 1} + N_{\phi 2}N_{\Phi 2} + N_{\phi 3}N_{\Phi 3}), \quad (4)$$

whereas the acquisition time for a unique volume V with dimensions $N_\phi N_\Phi N_f$ would be

$$T_0 = T_R N_\phi N_\Phi. \quad (5)$$

The time gain can thus be expressed as

$$G_T = 1 - \frac{T_{1+2+3}}{T_0} = 1 - \frac{(N_{\phi 1}N_{\Phi 1} + N_{\phi 2}N_{\Phi 2} + N_{\phi 3}N_{\Phi 3})}{N_\phi N_\Phi}. \quad (6)$$

This gain only depends on the ratios between the resolutions in the multiple acquisition case and the reference acquisition case. For instance, if $N_{\Phi i} = N_\Phi/3$, and $N_{\phi i} = N_\phi/3$ the whole acquisition time is three times shorter; if $N_{\Phi i} = N_\Phi/\sqrt{3}$, and $N_{\phi i} = N_\phi/\sqrt{3}$, the acquisition time remains unchanged but the SNR and resolution of the reconstructed volume will be improved. Finally if $N_{\Phi i} = N_\Phi$, and $N_{\phi i} = N_\phi$, the best resolution can be achieved by increasing the acquisition time to three breath-holdings of the patient: this triples the overall acquisition time and therefore also the resolution.

Studying the behavior of the acquisition process in terms of noise is not as easy as in terms of acquisition time: as a matter of fact, the noise variance in the final high resolution volume does not only depend on the acquisition process, but also on the combination strategy. However, acquiring an undersampled volume allows to reduce the noise variance when compared to the reference high-resolution volume, since the noise standard deviation σ is related to the volume dimensions as $\sigma = N_f\sqrt{N_\Phi N_\phi}$. According to the acquisition process, the low frequency coefficients of the k-space are acquired two or three times, leading to data redundancy and thus to an improvement of the SNR. Moreover, since the reconstruction method we propose includes a L2 regularization, noise will be further attenuated in the reconstruction process.

2.2. Combining the undersampled volumes

Having defined the acquisition scheme as in Section 2.1, our goal is now to reconstruct a unique high-resolution volume from three undersampled versions. This is a reconstruction or restoration problem and belongs to the family of inverse problems [4,10,19]. Since the data are discrete and the imaging system is band-limited, it can be proven that the solution is not unique and thus that the problem is ill-posed. For such problems, so-called generalized solutions are used such as the Wiener filter [1]. Moreover, most discrete inverse problems are ill-conditioned, i.e. noise in the data is amplified during the inversion process, which leads to unacceptable solutions. Therefore, approximate solutions are proposed and a priori information is introduced: the matter is to define a set of acceptable solutions (i.e. with limited error) and to choose among these solutions the best one according to an a priori criterion. This regularization generally consists in minimizing an objective function (also called energy function) of the form $Q + \lambda\Psi$, where Q measures the fidelity to the data, Ψ measures the regularity of the solution, and λ is a weighting factor of the regularization.

The a priori criterion Ψ has to be chosen according to the foreseen use of the reconstructed signal or image; the numerous applications that impose a precise edge localization, for example, call for the framework of edge-preserving regularization. In this framework, the term Ψ to be minimized is generally expressed as a sum over all sites (i.e. voxels in 3D images) of a regularization function (also called φ-function) applied to the neighbor differences. The choice of the φ-function determines the quality of the solution and the optimization method to be used; it has been addressed by many authors [6,9,15].

Here, the forseen application includes vessel segmentation and stenosis quantification. According to these considerations, it appears that the framework of edge-preserving regularization methods is well suited to the present problem.

The choice of the a priori criteria and the expression of the energy function are detailed in Section 3.

3. Edge-preserving reconstruction

The energy function to be minimized has the following form:

$$E = Q + \lambda\Psi, \quad (7)$$

where λ leads to a trade-off between Ψ, the regularization term, and Q, the fidelity to the data.

The expression of the energy function requires an accurate modeling of the anisotropic undersampling; this is developed below in Section 3.1. Section 3.2 presents the energy function in more details, and its convexity is discussed in Section 3.3. The choice of the optimization algorithm is justified in Section 3.4.

3.1. Modeling of the undersampling

Let I_{xy} be the image acquired with a decreased resolution along x and y; let I_{xz} and I_{yz} be the two other acquisitions defined in the same way. I_{xy} for instance is related to the wished high resolution image I_{HR} by

$$I_{xy}(x,y,z)=\sum_{k=0}^{N_x}\sum_{l=0}^{N_y} D_{xy}(k,l)I_{\mathrm{HR}}(x-k,y-l,z), \tag{8}$$

where D_{xy} is the undersampling operator along x and y. D_{xy} is separable:

$$D_{xy}(k,l)=D_x(k)D_y(l), \tag{9}$$

where D_x and D_y are the undersampling operators along x and y respectively.

Note that I_{xy}, I_{yz}, I_{xz}, and I_{HR} are the discrete Fourier transforms (DFTs) of k-spaces with different spectral supports: it seems reasonable to extend these supports to the smallest common cartesian support. This is achieved by interpolation and presented in Appendix A.

Let us now express the operators D_x, D_y and D_z. Let J_{HR} be the DFT of I_{HR}, and J_{xy} that of I_{xy}. The relation between J_{HR} and I_{HR} is

$$\begin{aligned}J(f_x,f_y,f_z)&=\sum_{x'=-\frac{N_x}{2}}^{\frac{N_x}{2}-1}\sum_{y'=-\frac{N_y}{2}}^{\frac{N_y}{2}-1}\sum_{z'=-\frac{N_z}{2}}^{\frac{N_z}{2}-1} F_{N_x}(f_x,x')F_{N_y}(f_y,y')\\&\quad\times F_{N_z}(f_z,z')I_{\mathrm{HR}}(x',y',z'),\end{aligned} \tag{10}$$

where F_N denotes the discrete Fourier transform matrix operator of size N:

$$F_N(n,k)=\frac{1}{N}\,\mathrm{e}^{-\mathrm{j}2\pi nk/N}\quad\text{with}$$

$$n,k=-\frac{N}{2}\cdots\frac{N}{2}-1. \tag{11}$$

The inverse DFT matrix operator is defined as

$$F_N^{-1}(n,k)=\mathrm{e}^{\mathrm{j}2\pi nk/N}\quad\text{with}$$

$$n,k=-\frac{N}{2}\cdots\frac{N}{2}-1. \tag{12}$$

As mentioned above, the acquisition process consists in acquiring a truncated k-space, i.e. I_{xy} is related to J_{HR} by

$$\begin{aligned}I_x(x,y,z)&=\sum_{f_x=-\frac{N_x'}{2}}^{\frac{N_x'}{2}-1}\sum_{f_y=-\frac{N_y'}{2}}^{\frac{N_y'}{2}-1}\sum_{f_z=-\frac{N_z}{2}}^{\frac{N_z}{2}-1} F_{N_x}^{-1}(x,f_x)F_{N_y}^{-1}(y,f_y)\\&\quad\times F_{N_z}^{-1}(z,f_z)J(f_x,f_y,f_z).\end{aligned} \tag{13}$$

Note the truncated summation limits in x and y directions. Eqs. (10) and (13) give the following relation between I_{HR} and I_{xy}:

$$\begin{aligned}I_x(x,y,z)&=\sum_{f_x=-\frac{N_x'}{2}}^{\frac{N_x'}{2}-1}\sum_{f_y=-\frac{N_y'}{2}}^{\frac{N_y'}{2}-1}\sum_{f_z=-\frac{N_z}{2}}^{\frac{N_z}{2}-1}[F_{N_x}^{-1}(x,f_x)\\&\quad\times F_{N_y}^{-1}(y,f_y)F_{N_z}^{-1}(z,f_z)\\&\quad\times\sum_{x'=-\frac{N_x}{2}}^{\frac{N_x}{2}-1}\sum_{y'=-\frac{N_y}{2}}^{\frac{N_y}{2}-1}\sum_{z'=-\frac{N_z}{2}}^{\frac{N_z}{2}-1} F_{N_x}(f_x,x')F_{N_y}(f_y,y')\\&\quad\times F_{N_z}(f_z,z')I(x',y',z')]\end{aligned} \tag{14}$$

from which it can be easily derived that the degradation operator is linear and separable.

Let us then consider the degradation operator along one direction at a time, for instance D_x along x, working on a one-dimensional vector (i.e. a row from the 3D image taken along direction x). We can then express the operator as a matrix within the framework of linear algebra. Under these conditions, the one-dimensional DFT of $I_x(\bullet,y,z)$ is

$$\mathrm{DFT}(I_x)=M_xF_xI_{\mathrm{HR}}, \tag{15}$$

where M_x is a $N_x \times N_x$ diagonal matrix:

$$\begin{aligned} &M_x(i,i) = 1 \quad \text{if } -\tfrac{N'_x}{2} + 1 \leqslant i \leqslant \tfrac{N'_x}{2} - 1, \\ &M_x(i,i) = 0.5 \quad \text{if } i = -\tfrac{N'_x}{2} \text{ or } i = \tfrac{N'_x}{2}, \\ &M_x(i,i) = 0 \quad \text{otherwise.} \end{aligned} \tag{16}$$

This expression with the 0.5 coefficient guarantees the consistency with Appendix A regarding the constraint of keeping real-valued images. Therefore

$$I_x = F_x^{-1} M_x F_x I_{\mathrm{HR}}. \tag{17}$$

Thus

$$I_x = D_x I_{\mathrm{HR}}, \tag{18}$$

where the degradation operator D_x is expressed as

$$D_x = F_x^{-1} M_x F_x. \tag{19}$$

The analytic expression of D_x is provided in Appendix B and it can be easily seen that it is a circulant operator. The operators D_y and D_z can be expressed in a similar way. The whole 3D problem can also be expressed with matrix operators, but it requires to work on vector data (i.e. to put the 3D image matrix into a large vector) and to transform the operators D_x, D_y and D_z into large matrix operators, according to [25,27]. In the following we will deal with such vectors and matrices and use bold font to distinguish them from the operators working in one dimension. For example, $\mathbf{D}_x$ denotes the "big" matrix working on the "big" vector $\mathbf{I}_{\mathrm{HR}}$ obtained by concatenation of all the images values into a "big" column vector; the way to compute $\mathbf{D}_x$ from D_x is detailed in [25,27]. Such linear algebra notations allow to express for example Eq. (8) with matrix operators:

$$\mathbf{I}_{xy} = \mathbf{D}_x \mathbf{D}_y \mathbf{I}_{\mathrm{HR}}. \tag{20}$$

3.2. The energy function

3.2.1. Fidelity to the data

The matter is to minimize the sum of the quadratic errors between the reconstructed image and the data:

$$\begin{aligned} Q = &\|\mathbf{D}_{xy}\mathbf{I}_{\mathrm{rec}} - \mathbf{I}_{xy}\|^2 + \|\mathbf{D}_{yz}\mathbf{I}_{\mathrm{rec}} - \mathbf{I}_{yz}\|^2 \\ &+ \|\mathbf{D}_{zx}\mathbf{I}_{\mathrm{rec}} - \mathbf{I}_{zx}\|^2, \end{aligned} \tag{21}$$

where $\mathbf{D}_{xy}$, $\mathbf{D}_{yz}$ and $\mathbf{D}_{zx}$ are the "big" undersampling operators obtained from those of Section 3.1, $\|.\|$ represents the quadratic norm, I_{rec} is the high-resolution image at current iteration (the optimization of E is based on an iterative method), $\mathbf{I}_{xy}$, $\mathbf{I}_{yz}$ and $\mathbf{I}_{xz}$ are the low-resolution input images put in vector form.

3.2.2. Regularization term

As mentioned in Section 2.2, the regularization term Ψ is defined as a φ-function of the neighbor differences; here the chosen φ-function is called ψ (to avoid confusion with the phase encoding directions) and is applied to the first order neighbor differences. Let Δ_N be the $N \times N$ matrix operator of the neighbor differences. Since data are acquired in the spectral domain, and the DFT implicitly assumes the periodicity of both signal and spectrum, the border conditions are chosen here to be periodic ones, leading to

$$\Delta_N = \begin{pmatrix} 1 & 0 & \cdots & 0 & -1 \\ -1 & 1 & & & 0 \\ 0 & \ddots & \ddots & & \vdots \\ \vdots & & \ddots & \ddots & 0 \\ 0 & \cdots & 0 & -1 & 1 \end{pmatrix}. \tag{22}$$

The regularization term Ψ takes the following form:

$$\begin{aligned} \Psi = &\|\psi(\boldsymbol{\Delta}_y \mathbf{I}_{\mathrm{rec}})\|_1 + \|\psi(\boldsymbol{\Delta}_x \mathbf{I}_{\mathrm{rec}})\|_1 \\ &+ \|\psi(\boldsymbol{\Delta}_z \mathbf{I}_{\mathrm{rec}})\|_1, \end{aligned} \tag{23}$$

where $\boldsymbol{\Delta}_x$, $\boldsymbol{\Delta}_y$ and $\boldsymbol{\Delta}_z$ are the "big" matrices obtained from Δ_N according to Section 3.1 and to [25,27], and $\|\|_1$ denotes the L1 norm.

The choice of the potential function ψ results from a trade-off: the ideal edge-preserving potential functions are those which have an asymptotic flat behavior towards infinity, such as that of Blake and Zisserman [6], Geman and McClure [16], or Hebert and Leahy [17]; unfortunately, all these functions are not convex and therefore compel to use time-consuming optimization algorithms.

On the contrary, the function that is best suited to fast algorithms such as the conjugate gradient algorithm is that of Tikhonov (quadratic function), but unfortunately it smoothes discontinuities.

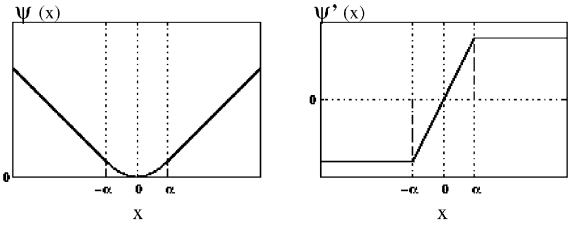

Fig. 2. Left: the Huber potential function. Right: its derivative.

Therefore we chose the Huber potential function [5], which is convex and has an asymptotic linear behavior towards infinity which allows us to preserve the discontinuities in a satisfactory way. When applied to the first order neighbor differences, the Huber potential function makes areas with small local differences more homogeneous, while preserving discontinuities i.e. strong differences between neighbor voxels.

The Huber function (Fig. 2) can be expressed as [5]

$$\begin{cases} \psi(x) = x^2 & \text{if } |x| \leqslant \alpha, \\ \psi(x) = 2\alpha|x| - \alpha^2 & \text{if } |x| > \alpha \end{cases} \tag{24}$$

and its derivative:

$$\begin{cases} \psi'(x) = 2x & \text{if } |x| \leqslant \alpha, \\ \psi'(x) = 2\alpha \operatorname{sign}(x) & \text{if } |x| > \alpha. \end{cases} \tag{25}$$

The parameter α allows us to tune the function behavior as follows: the smaller α, the more the function resembles the $|x|$ function, thus the better the image contours are preserved; on the contrary, the larger α, the more the function resembles the x^2 function, thus the more the contours are smoothed [20] and the better the noise is filtered.

3.3. Study of the convexity

The convergence problem arises as soon as the energy function is not convex. Indeed, in this case, the conventional optimization algorithms can only provide a local minimizer of the energy function. That is why the convexity of the energy function is of primary importance. We show in [27] that the energy function is convex, but that the strict convexity of the energy function depends on the image considered, because of the non-linearity of the regularization function.

3.4. Choice of the minimization algorithm

The convexity of the energy function allows us to use a simple deterministic algorithm. Among the existing algorithms, we choose to use the conjugate gradient algorithm for its simplicity and efficiency. Particularly, if the energy function can be expressed as a quadratic form, the conjugate gradient algorithm has interesting convergence properties; our energy function is not strictly quadratic but is composed of several quadratic or nearly quadratic terms, which lets us think that the convergence may be acceptable. The conjugate gradient algorithm requires to evaluate at each iteration not only the energy $E(I_{\text{rec}})$ as a function of the current image I_{rec}, but also its partial derivatives $\bigtriangledown E(I_{\text{rec}})_{i,j}$ with respect to the image intensity $I_{\text{rec}}(i,j)$ of each pixel of the current image. This is provided in Appendix C.

4. Half-quadratic regularization

In this section, we propose an alternative method to solve the reconstruction problem. It is based on the notion of half-quadratic regularization and on the ARTUR and LEGEND algorithms, developed in [8].

4.1. Principle

The main idea of these approaches consists in introducing an auxiliary variable b and to modify the non quadratic objective function E into a half-quadratic function E^* such that [8,14]

$$E(I_{\text{rec}}) = \min_b E^*(I_{\text{rec}}, b), \tag{26}$$

where b represents the discontinuities, also called line process. Hereafter, we assume that $E(I_{\text{rec}})$ can be written as

$$E(I_{\text{rec}}) = \|DI_{\text{rec}} - I_{\text{data}}\|^2 + \lambda \left[\sum_k \psi((\Delta_x I_{\text{rec}})_k) + \sum_k \psi((\Delta_y I_{\text{rec}})_k) + \sum_k \psi((\Delta_z I_{\text{rec}})_k) \right], \tag{27}$$

where ψ is a regularization function, $\Delta_x I_{\text{rec}}$, $\Delta_y I_{\text{rec}}$ and $\Delta_z I_{\text{rec}}$ are the neighbor differences in each spatial direction, I_{data} is the observed image and D is

the degradation operator. The auxiliary variable can be defined in two ways. In the first one [8], it is assumed that $\psi(\sqrt{(u)})$ is strictly convex and $b \in [0,1]$ is defined such that $\psi(u) = \inf_b bu^2 + \xi(b)$. In the second approach [2], it is assumed that $u^2 - \psi(u)$ is strictly convex, and $b \in [0,+\infty]$ is defined such that $\psi(u) = \inf_b (b-u)^2 + \xi(b)$. The ARTUR algorithm is based on the first approach, while LEGEND is based on the second one.

For regularization functions which are convex, non-bounded and with bounded first derivative, it can be proved that $E^*(I_{\text{rec}}, b)$ is quadratic in I_{rec} for fixed b, and $E^*(I_{\text{rec}}, b)$ is convex in b for fixed I_{rec}; the value of b which minimizes $E^*(I_{\text{rec}}, b)$ for fixed I_{rec} is known analytically.

The algorithms rely on these properties and alternatively minimize E^* in b for fixed I_{rec} and in I_{rec} for fixed b.

Both problems can be expressed with linear algebra and amount to solve a linear system of the form $\mathbf{A}\mathbf{I}_{\text{rec}} = \mathbf{c}$ (see [27]). In ARTUR, $\mathbf{A}$ depends on the iteration, while it is constant in LEGEND. Moreover, in the case of LEGEND $\mathbf{A}$ is invertible, while this is questionable in the case of ARTUR. For these reasons, we chose to express the problem using LEGEND, firstly in the spatial domain, and then alternatively in the spectral domain, for reasons that will be explained in Section 4.2.

4.2. LEGEND algorithm in the spatial domain

According to the principle explained above, the algorithm has to compute $\mathbf{I}^n_{\text{rec}}$ by solving $\nabla E = 0$ for fixed $\mathbf{b}^n_x$, $\mathbf{b}^n_y$ and $\mathbf{b}^n_z$, and to compute the auxiliary variables $\mathbf{b}^{n+1}_x$, $\mathbf{b}^{n+1}_y$ and $\mathbf{b}^{n+1}_z$ as functions of $\mathbf{I}^n_{\text{rec}}$ (in these expressions, n denotes the iteration number).

It has been shown in [8] that $\mathbf{b}^{n+1}_x$ can be expressed as

$$(\mathbf{b}^{n+1}_x)_k = \left[1 - \frac{\psi'[(\Delta_x \mathbf{I}^n_{\text{rec}})_k]}{2(\Delta_x \mathbf{I}^n_{\text{rec}})_k}\right](\Delta_x \mathbf{I}^n_{\text{rec}})_k. \tag{28}$$

For the first computation, we have to derive an expression of $\nabla E = 0$. The regularization term can be written as

$$\Psi(I_{\text{rec}}) = \inf_{b_x,b_y,b_z} [\Psi^*(I_{\text{rec}}, b_x, b_y, b_z)] \tag{29}$$

with

$$\begin{aligned}\Psi^* = &\sum_i \sum_j \sum_k (b_y(i,j,k) - (I_{\text{rec}}(i,j,k)\\ &-I_{\text{rec}}(i-1,j,k)))^2 + \xi(b_y(i,j,k))\\ &+\sum_i \sum_j \sum_k (b_x(i,j,k) - (I_{\text{rec}}(i,j,k)\\ &-I_{\text{rec}}(i,j-1,k)))^2 + \xi(b_x(i,j,k))\\ &+\sum_i \sum_j \sum_k (b_z(i,j,k) - (I_{\text{rec}}(i,j,k)\\ &-I_{\text{rec}}(i,j,k-1)))^2 + \xi(b_z(i,j,k))\end{aligned} \tag{30}$$

i.e., using matricial notations:

$$\begin{aligned}\Psi^* = &(\mathbf{b}_x - \Delta_x \mathbf{I}_{\text{rec}})^{\mathrm{T}}(\mathbf{b}_x - \Delta_x \mathbf{I}_{\text{rec}})\\ &+(\mathbf{b}_y - \Delta_y \mathbf{I}_{\text{rec}})^{\mathrm{T}}(\mathbf{b}_y - \Delta_y \mathbf{I}_{\text{rec}})\\ &+(\mathbf{b}_z - \Delta_z \mathbf{I}_{\text{rec}})^{\mathrm{T}}(\mathbf{b}_z - \Delta_z \mathbf{I}_{\text{rec}})\\ &+\sum_k [\xi(\mathbf{b}_x(k)) + \xi(\mathbf{b}_y(k)) + \xi(\mathbf{b}_z(k))].\end{aligned} \tag{31}$$

The partial derivatives of Ψ^* with respect to $\mathbf{I}_{\text{rec}}$ are

$$\begin{aligned}\nabla\Psi^* = &2[\Delta_x^{\mathrm{T}}\Delta_x \mathbf{I}_{\text{rec}} - \Delta_x^{\mathrm{T}}\mathbf{b}_x + \Delta_y^{\mathrm{T}}\Delta_y \mathbf{I}_{\text{rec}}\\ &-\Delta_y^{\mathrm{T}}\mathbf{b}_y + \Delta_z^{\mathrm{T}}\Delta_z \mathbf{I}_{\text{rec}} - \Delta_z^{\mathrm{T}}\mathbf{b}_z]\end{aligned} \tag{32}$$

from which we derive the following expression of $\nabla\mathbf{E}^*$:

$$\begin{aligned}\nabla\mathbf{E}^* = &2[\mathbf{D}_{xy}^{\mathrm{T}}\mathbf{D}_{xy} + \mathbf{D}_{yz}^{\mathrm{T}}\mathbf{D}_{yz} + \mathbf{D}_{xz}^{\mathrm{T}}\mathbf{D}_{xz}\\ &+\lambda(\Delta_x^{\mathrm{T}}\Delta_x + \Delta_y^{\mathrm{T}}\Delta_y + \Delta_z^{\mathrm{T}}\Delta_z)]\mathbf{I}_{\text{rec}}\\ &-2[\mathbf{D}_{xy}^{\mathrm{T}}\mathbf{I}_{xy} + \mathbf{D}_{yz}^{\mathrm{T}}\mathbf{I}_{yz} + \mathbf{D}_{xz}^{\mathrm{T}}\mathbf{I}_{xz}\\ &+\lambda(\Delta_x^{\mathrm{T}}\mathbf{b}_x + \Delta_y^{\mathrm{T}}\mathbf{b}_y + \Delta_z^{\mathrm{T}}\mathbf{b}_z)]\end{aligned} \tag{33}$$

and $\nabla E^* = 0$ is equivalent to

$$\begin{aligned}&[\mathbf{D}_{xy}^{\mathrm{T}}\mathbf{D}_{xy} + \mathbf{D}_{yz}^{\mathrm{T}}\mathbf{D}_{yz} + \mathbf{D}_{xz}^{\mathrm{T}}\mathbf{D}_{xz}\\ &\quad+\lambda(\Delta_x^{\mathrm{T}}\Delta_x + \Delta_y^{\mathrm{T}}\Delta_y + \Delta_z^{\mathrm{T}}\Delta_z)]\mathbf{I}_{\text{rec}}\\ &=[\mathbf{D}_{xy}^{\mathrm{T}}\mathbf{I}_{xy} + \mathbf{D}_{yz}^{\mathrm{T}}\mathbf{I}_{yz} + \mathbf{D}_{xz}^{\mathrm{T}}\mathbf{I}_{xz}\\ &\quad+\lambda(\Delta_x^{\mathrm{T}}\mathbf{b}_x + \Delta_y^{\mathrm{T}}\mathbf{b}_y + \Delta_z^{\mathrm{T}}\mathbf{b}_z)]\end{aligned} \tag{34}$$

which is an expression of the form $\mathbf{A}\mathbf{I}^{n+1}_{\text{rec}} = \mathbf{c}$ with $\mathbf{A}$ constant and where $\mathbf{c}$ depends on $\mathbf{I}^n_{\text{rec}}$.

As mentioned in Section 3.1, D_x and Δ_x are circulant operators; it is well known that if a matrix C is circulant, then so is $C^{\mathrm{T}}C$, and that the sum of circulant matrices is also circulant. Thus, $\mathbf{A}$ is also circulant. Because of the interesting properties of circulant matrices in the Fourier domain (they become diagonal matrices), we propose to express the problem in the spectral domain in Section 4.3.

4.3. LEGEND algorithm in the spectral domain

Equation $\mathbf{A}\mathbf{I}_{\mathrm{rec}}^{n+1} = \mathbf{c}$ can be rewritten as

$$\mathbf{F}_x\mathbf{F}_y\mathbf{F}_z\mathbf{A}\mathbf{F}_x^{-1}\mathbf{F}_y^{-1}\mathbf{F}_z^{-1}\mathbf{J}_{\mathrm{rec}}^{n+1} = \mathbf{F}_x\mathbf{F}_y\mathbf{F}_z\mathbf{c}, \tag{35}$$

where $\mathbf{J}_{\mathrm{rec}}^{n+1}$ is the discrete Fourier transform of $\mathbf{I}_{\mathrm{rec}}^{n+1}$.

Let $\mathbf{H}_{xyz}$ be defined as

$$\mathbf{H}_{xyz} = \mathbf{F}_x\mathbf{F}_y\mathbf{F}_z\mathbf{A}\mathbf{F}_x^{-1}\mathbf{F}_y^{-1}\mathbf{F}_z^{-1}. \tag{36}$$

It can be written as

$$\mathbf{H}_{xyz} = \mathbf{H}_{xy} + \mathbf{H}_{yz} + \mathbf{H}_{xz} + \mathbf{H}_x + \mathbf{H}_y + \mathbf{H}_z, \tag{37}$$

where for example $\mathbf{H}_{xy}$ only operates along directions x et y, and so on. Since matrices operating along different directions commute [27], we have

$$\mathbf{H}_{xy} = \mathbf{F}_x\mathbf{D}_x^{\mathrm{T}}\mathbf{D}_x\mathbf{F}_x^{-1}\mathbf{F}_y\mathbf{D}_y^{\mathrm{T}}\mathbf{D}_y\mathbf{F}_y^{-1} \tag{38}$$

as well as

$$\mathbf{H}_x = \lambda\mathbf{F}_x\mathbf{\Delta}_x^{\mathrm{T}}\mathbf{\Delta}_x\mathbf{F}_x^{-1} \tag{39}$$

and similar expressions can be derived for $\mathbf{H}_{yz}$, $\mathbf{H}_{xz}$, $\mathbf{H}_y$ and $\mathbf{H}_z$. From these expressions it can be easily shown that all elements of $\mathbf{H}_{xyz}$ are diagonal, and thus so is $\mathbf{H}_{xyz}$. It has been proven in [27] that $\mathbf{H}_{xyz}$ is also invertible. Eq. (35) can therefore be solved by scalar divisions in the Fourier domain:

$$\mathbf{J}_{\mathrm{rec}}^{n+1}(k) = \frac{(\mathbf{F}_x\mathbf{F}_y\mathbf{F}_z\mathbf{c})(k)}{\mathbf{H}_{xyz}(k,k)}. \tag{40}$$

Let us now consider the term $\mathbf{F}_x\mathbf{F}_y\mathbf{F}_z\mathbf{c}$:

$$\begin{aligned}\mathbf{F}_x\mathbf{F}_y\mathbf{F}_z\mathbf{c} = {} & \mathbf{F}_x\mathbf{D}_x^{\mathrm{T}}\mathbf{F}_x^{-1}\mathbf{F}_y\mathbf{D}_y^{\mathrm{T}}\mathbf{F}_y^{-1}\mathbf{J}_{xy} \\ & +\mathbf{F}_y\mathbf{D}_y^{\mathrm{T}}\mathbf{F}_y^{-1}\mathbf{F}_z\mathbf{D}_z^{\mathrm{T}}\mathbf{F}_z^{-1}\mathbf{J}_{yz} \\ & +\mathbf{F}_x\mathbf{D}_x^{\mathrm{T}}\mathbf{F}_x^{-1}\mathbf{F}_z\mathbf{D}_z^{\mathrm{T}}\mathbf{F}_z^{-1}\mathbf{J}_{xz} \\ & +\lambda[\mathbf{F}_x\mathbf{\Delta}_x^{\mathrm{T}}\mathbf{F}_x^{-1}\beta_x + \mathbf{F}_y\mathbf{\Delta}_y^{\mathrm{T}}\mathbf{F}_y^{-1}\beta_y \\ & +\mathbf{F}_z\mathbf{\Delta}_z^{\mathrm{T}}\mathbf{F}_z^{-1}\beta_z],\end{aligned} \tag{41}$$

where β_x, β_y and β_z are the DFT of $\mathbf{b}_x$, $\mathbf{b}_y$ and $\mathbf{b}_z$ respectively. Since Δ_x is a circulant matrix, it follows that $F_x\Delta_x^{\mathrm{T}}F_x^{-1}$ is diagonal, and its diagonal elements are expressed as the DFT of the series $\Delta_x(m-n)$ for $m-n$ varying from $-N_x/2$ to $N_x/2-1$ (up to N_x):

$$(F_x\Delta_x^{\mathrm{T}}F_x^{-1})(m,m) = 1 - \mathrm{e}^{\mathrm{j}2\pi m/N_x}. \tag{42}$$

Let us denote this matrix by P_x; similar expressions are obtained for P_y and P_z. Let us also note $\mathbf{J}_{xyz}$ the constant term:

$$\begin{aligned}\mathbf{J}_{xyz} = {} & \mathbf{F}_x\mathbf{D}_x^{\mathrm{T}}\mathbf{F}_x^{-1}\mathbf{F}_y\mathbf{D}_y^{\mathrm{T}}\mathbf{F}_y^{-1}\mathbf{J}_{xy} \\ & +\mathbf{F}_y\mathbf{D}_y^{\mathrm{T}}\mathbf{F}_y^{-1}\mathbf{F}_z\mathbf{D}_z^{\mathrm{T}}\mathbf{F}_z^{-1}\mathbf{J}_{yz} \\ & +\mathbf{F}_x\mathbf{D}_x^{\mathrm{T}}\mathbf{F}_x^{-1}\mathbf{F}_z\mathbf{D}_z^{\mathrm{T}}\mathbf{F}_z^{-1}\mathbf{J}_{xz}.\end{aligned} \tag{43}$$

Finally we get

$$\mathbf{J}_{\mathrm{rec}}^{n+1}(k) = \frac{\mathbf{J}_{xyz}(k) + \lambda[\mathbf{P}_x(k,k)\beta_x^{n+1}(k) + \mathbf{P}_y(k,k)\beta_y^{n+1}(k) + \mathbf{P}_z(k,k)\beta_z^{n+1}(k)]}{\mathbf{H}_{xyz}(k,k)} \tag{44}$$

The adaptation of LEGEND to our problem consists in iterating the following steps:

- Compute $\mathbf{b}_x^{n+1}$, $\mathbf{b}_y^{n+1}$, $\mathbf{b}_z^{n+1}$ using Eq. (28).
- Compute the DFT β_x^{n+1}, β_y^{n+1}, β_z^{n+1} of $\mathbf{b}_x^{n+1}$, $\mathbf{b}_y^{n+1}$, $\mathbf{b}_z^{n+1}$.
- Compute $\mathbf{J}_{\mathrm{rec}}^{n+1}$ according to

$$\begin{aligned}(\mathbf{J}_{\mathrm{rec}}^{n+1})_k = {} & (K_1)_k + (K_2)_k(\beta_x^{n+1})_k + (K_3)_k(\beta_y^{n+1})_k \\ & +(K_4)_k(\beta_z^{n+1})_k\end{aligned} \tag{45}$$

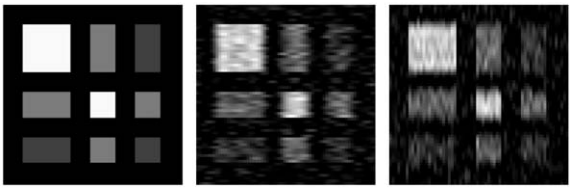

Fig. 3. Left: the high-resolution phantom, Middle: simulation of the noisy acquisition with undersampling along x, Right: simulation of the noisy acquisition with undersampling along y. Undersampling ratio is here 64/20.

with

$$(K_1)_k = \frac{(\mathbf{J}_{xyz})_k}{(\mathbf{H}_{xyz})_{k,k}},$$

$$(K_2)_k = \lambda \frac{(\mathbf{P}_x)_{k,k}}{(\mathbf{H}_{xyz})_{k,k}},$$

$$(K_3)_k = \lambda \frac{(\mathbf{P}_y)_{k,k}}{(\mathbf{H}_{xyz})_{k,k}},$$

$$(K_4)_k = \lambda \frac{(\mathbf{P}_z)_{k,k}}{(\mathbf{H}_{xyz})_{k,k}}. \quad (46)$$

- Compute the inverse DFT $\mathbf{I}_{\text{rec}}^{n+1}$ of $\mathbf{J}_{\text{rec}}^{n+1}$.

Note that in Cartesian coordinates, the DFT benefits of FFT algorithms.

5. Validation and discussion

In this section we evaluate the reconstruction on a phantom in terms of edge preservation and fidelity to the data. This evaluation is performed on a set of two anisotropic 2D images coded on 8 bits, each with a decreased resolution along one direction.

Fig. 3 presents the high-resolution phantom, composed of areas with constant intensities, as well as both anisotropic simulated acquisitions (after addition of Gaussian white noise with standard deviation 10% of the maximum grey level, and zero-padding interpolation with an undersampling ratio of 3.2).

5.1. Comparison of both reconstruction algorithms: conjugate gradient and LEGEND

We first compare the two proposed algorithms in terms of computation time, convergence speed and sensitivity to the initialization.

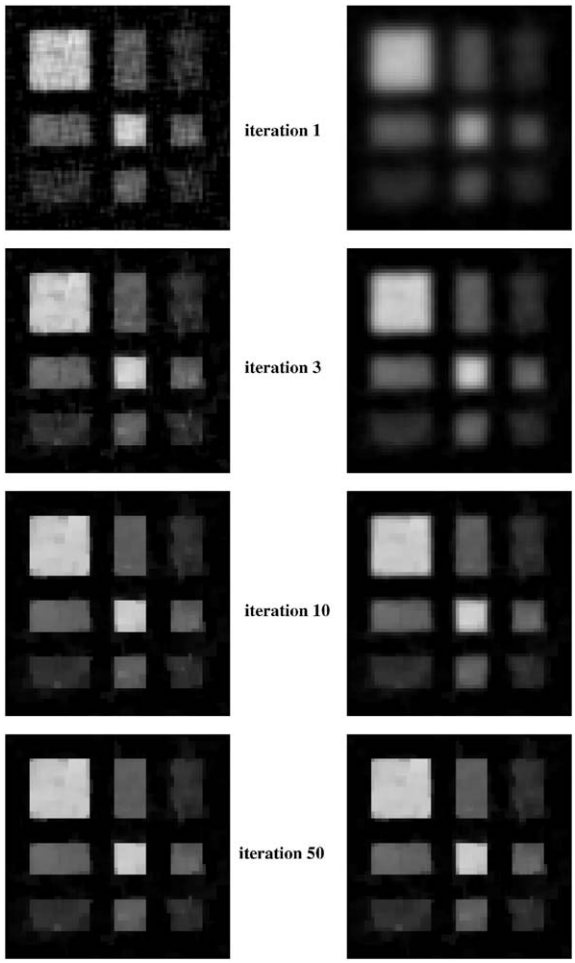

Fig. 4. Evolution of the solution using the conjugate gradient method (left) and LEGEND (right). The last iteration corresponds to the convergence.

Fig. 4 illustrates a few iterations of the two algorithms applied on the images of Fig. 3. The energy variation is shown in Fig. 5. These results were obtained for a null initialization and with parameters $\lambda = 10$ and $\alpha = 2$ (for images with 256 grey levels).

For the conjugate gradient method, the first iteration corresponds to a non-regularized solution, which is illustrated in Fig. 4. At this step, the data fidelity term is therefore minimal while the regularization term can be anything. During the iterations, the regularization has an increased influence, leading to a smoother solution, as can be seen in Fig. 5.

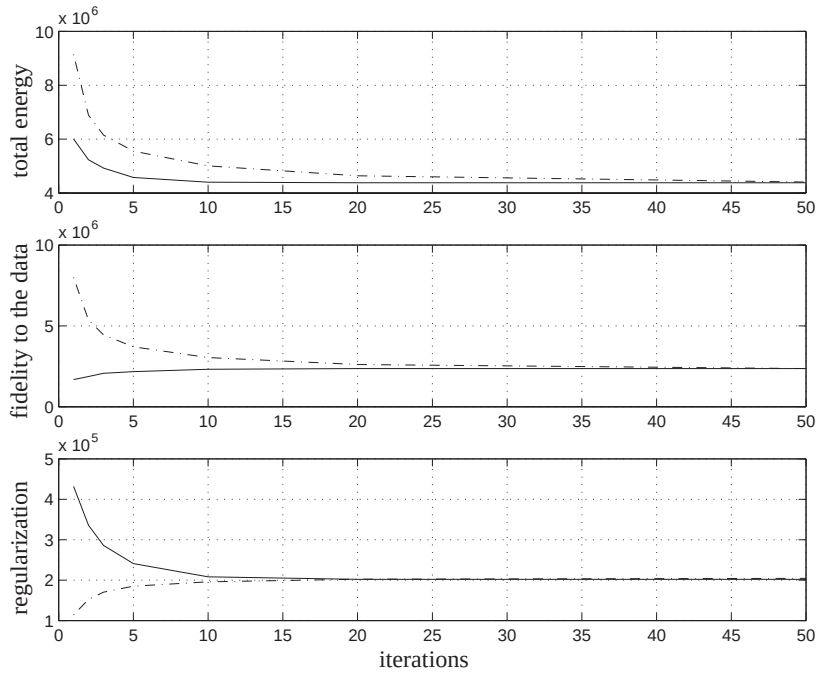

Fig. 5. From top to bottom: variation of the total energy, of the data fidelity term and of the regularization term. Plain line: conjugate gradient; dotted line: LEGEND.

For LEGEND, the discontinuities are progressively introduced [8]. The first iteration corresponds to a quadratic regularization, generally quite far from the data. During the iterations, the data fidelity term decreases while the regularization energy increases. This behavior can be observed in Figs. 4 and 5.

Although on this example LEGEND needs more iterations, this is not always the case and nothing can be concluded on this point. For instance on the example of the aorta shown below in Section 6, a faster convergence is achieved using LEGEND.

However, when comparing the computation times instead of the number of iterations, it appears that LEGEND is faster (see Fig. 6). Both methods have been programmed in MATLAB.

Concerning the initialization, if it is chosen as the non-regularized solution, we avoid one iteration with the conjugate gradient. On the contrary LEGEND does not converge as easily as when starting from a null initialization. If the initialization is chosen as the Tikhonov regularization, then LEGEND has a lower initial energy than with a null initialization, and the conjugate gradient has a similar convergence as in the other cases. If the initialization is the average of both acquisitions, then both algorithms behave well. Finally, we also tested the methods with a random initialization, which results in a slower convergence for LEGEND. From all these tests, it seems that the conjugate gradient is slightly less sensitive to the initialization than LEGEND. However, the computation time is always lower for LEGEND (except in the case of a random initialization). We conclude that it is reasonable to choose either a null initialization, or the average of both acquisitions.

5.2. *Influence of the parameters λ and α*

Fig. 7-left shows the reconstruction result for $\lambda = 0$, which corresponds to a least-square reconstruction. This least-square reconstruction can be improved by considering prior regularization constraints.

Fig. 7-right shows the regularized reconstruction result for α much larger than the maximum grey level value: the function is then equivalent in the domain

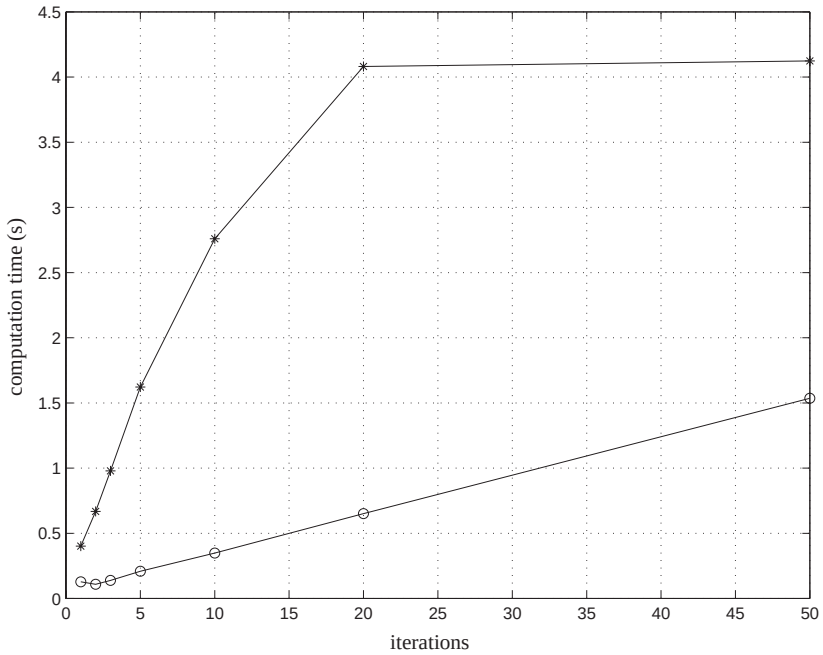

Fig. 6. Evolution of the computation time as a function of the number of iterations,for the conjugate gradient (∗) and LEGEND (○).

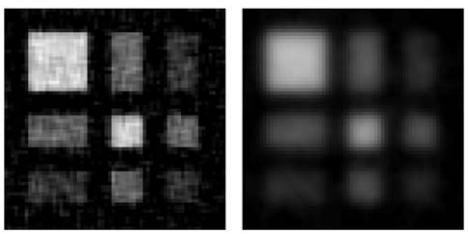

Fig. 7. Left: reconstruction result for $\lambda = 0$. Right: reconstruction result for $\alpha \to \infty$.

Fig. 8. Results obtained for various values of λ, with $\alpha = 2$: left, $\lambda = 0.5$; middle, $\lambda = 2$; right, $\lambda = 10$.

of interest to the Tikhonov function (i.e. the purely quadratic function). The smoothing is thus a global smoothing, independently of the neighbor difference values with respect to the image intensity range. Therefore, edges are of worse quality than in a high resolution acquisition.

In Fig. 8 we present some results obtained for different values of λ with constant α. These results confirm the expected behavior of the regularization: when λ increases, the reconstruction result becomes smoother, but contours remain equally sharp.

The parameter α can be seen intuitively as a threshold under which the neighbor differences are considered as noise and have to be smoothed, and above which they are considered as contour information and have to be preserved.

A convenient way to study the influence of the parameter α can be to compare results obtained with a constant product $\alpha \cdot \lambda$; indeed the slope of the linear part of the $\psi(x)$ function defined in Section 3.2 (Eq. (24)) is 2α and varies with α, and thus the slope of $\lambda\psi(x)$ is $2\lambda\alpha$. This is illustrated in Fig. 9: when the product $\alpha \cdot \lambda$ is not constant, the study of the influence of α is disturbed by the variation of the weighting

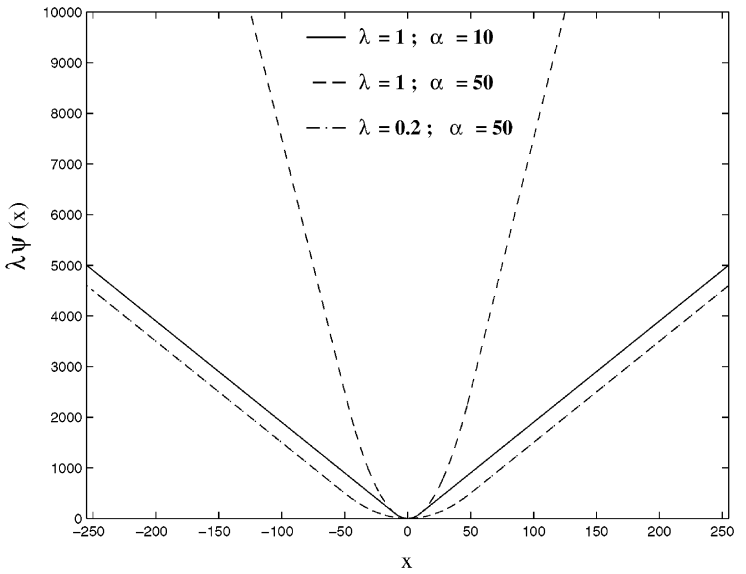

Fig. 9. Illustration of the constraint $\alpha \cdot \lambda =$ constant for the study of the influence of α.

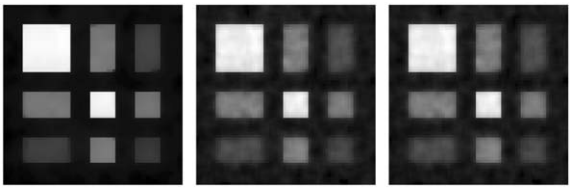

Fig. 10. Reconstruction result for various values of α, with $\alpha \cdot \lambda = constant = 50$: left, $\alpha = 2$, middle, $\alpha = 10$, right, $\alpha = 20$.

between the terms Q and Ψ. This is only valid for small values of α, since for large values of α the offsets of both straight lines greatly differ from each other.

Taking this remark into account, we present in Fig. 10 the results obtained for various values of α, the product $\alpha \cdot \lambda$ being constant.

Whereas the contours delineating well contrasted areas are well preserved, the edges between less contrasted areas are characterized by neighbor differences smaller than α and are thus smoothed as noise, when α is too large.

5.3. Estimation of the optimal hyperparameters

Taking into account the specificity of our application, we define quality measures for the reconstruction. These measures include, among others, the noise variance in homogeneous areas (both in the background and in bright objects), as a smoothness measure, and the power at sites known as edges, as an edge sharpness measure. Two of them are represented in Fig. 11 together with a more global measure: the power of the difference between the reference image and the reconstruction. The confrontation of these curves allows to define an optimal area for the couple of parameters, shown in Fig. 11 (bottom right).

In a second step, the same kind of evaluation was performed on a simulated vessel with stenosis, oriented along different orientations. The same measures as above cannot be used, since the object intensity is not strictly constant and the edges are not as sharp as in the simple model used above. However the commonly used measure of the root-mean-square difference between the reference and the reconstruction can still be used: in Fig. 12 we show slices of a vessel that is approximatively "aligned along k-space axes" and of an "oblique" vessel, together with the corresponding error with respect to the reference as a function of α and λ.

These measures confirm the results obtained with the first set of evaluation images; moreover, they show that the optimal parameters are not strongly dependent

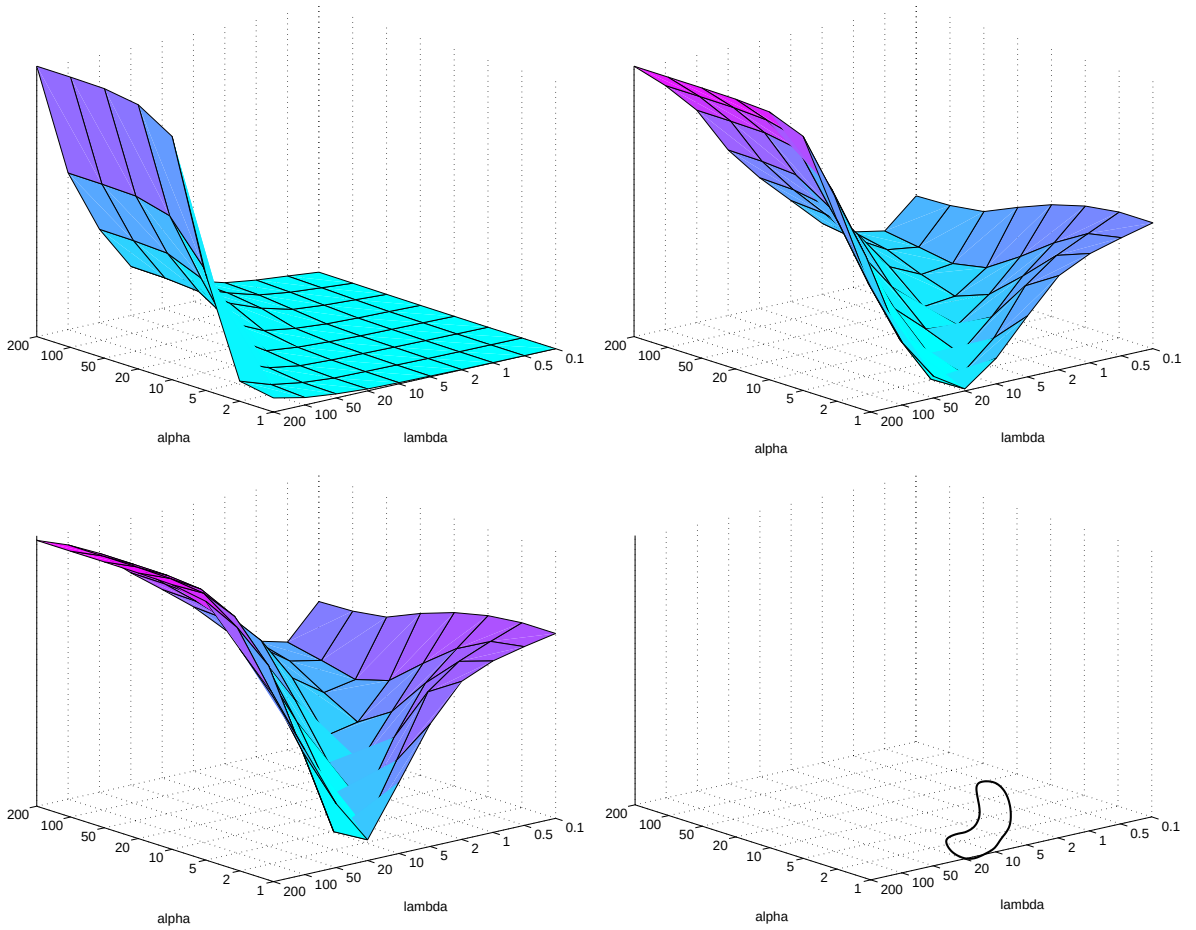

Fig. 11. Quality measures as a function of α and λ. Top left: the inverse edges power (logarithmical scale). Top right: the power of the difference image. Bottom left: the noise variance in the background. Bottom right: the optimal area for the set of parameters (α, λ) obtained from the confrontation of all quality measures.

on the orientation of the edges. However, we showed that the reconstruction results can be improved by performing so-called "double oblique" acquisitions, in order to align roughly the vessel axis along one of the k-space axes [27].

5.4. Summary

This section showed experimentally the need to regularize while preserving the edges. It clearly appears that a least-square reconstruction is not sufficient; moreover, the conventional Tikhonov φ-function is not well suited to the application considered in this paper since it smoothes the edges. These are the reasons why the non-linear regularizing Huber function was chosen; optimal values for the two parameters were determined and tested on synthetic vessel images.

Robustness of the method with respect to the parameters α and λ was established experimentally from the shape of the curves of Fig. 11: indeed within the "optimal area" the curves are relatively flat, thus a small change of one parameter within this area may not imply visible changes in the reconstruction. As a conclusion, λ may be chosen not to far from the unity and α much smaller than the image range. We suggest

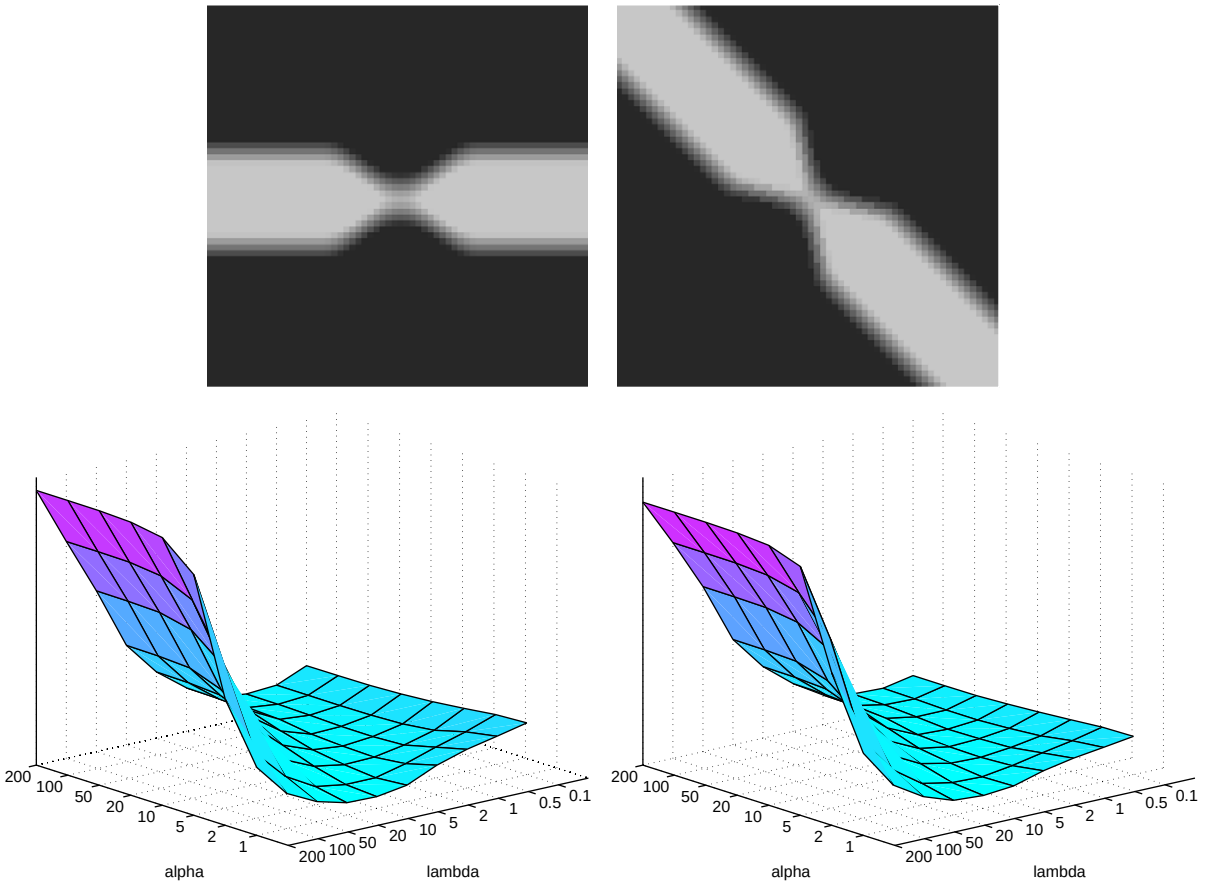

Fig. 12. Top: the two sample simulated vessel slices that were used for estimating the optimal parameters. Bottom: the power of the error image as a function of λ and α (left: for the "straight" vessel, right: for the "oblique" vessel).

to use for example $\alpha \simeq 2$ and $\lambda \simeq 5$ for an image ranging from 0 to 255.

6. First results on real data

The method was evaluated on five sets of undersampled MR volumes of the aorta (two sets) and of the carotid artery (three sets). For each of the five patients, orthogonal volumes with complementary spatial resolutions were acquired. Each volume was acquired during injection of gadolinium and breath-holding of the patient, using a 1.5 T clinical system (Signa, GE Medical Systems, Milwaukee, WI). Results obtained on the aorta of one patient and on the carotid artery of one patient are presented, respectively in Sections 6.1 and 6.2.

6.1. Aorta example

The volumes were acquired with a 3D gradient-echo sequence (parameters $T_R = 4.7$ ms and $T_E = 1.8$ ms). The voxel size of the first volume is, respectively in x, y and z (x denoting the supero-inferior direction of the human body, y the left-right one, and z the antero-posterior direction), $0.98 \times 2.23 \times 4$ mm^3, and that of the second volume, $4 \times 2.23 \times 0.98$ mm^3. The voxel size of the final recovered volume including the ascending aorta is $0.98 \times 2.23 \times 0.98$ mm^3. Obtaining the same spatial resolution in a single equivalent

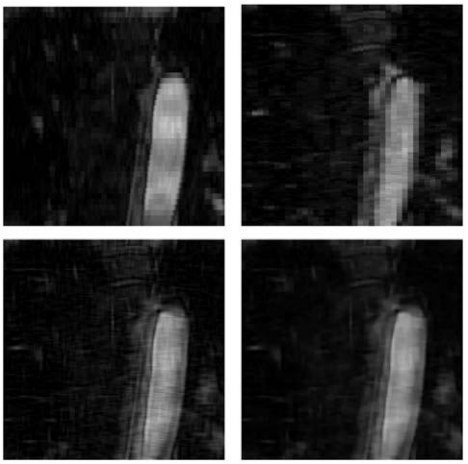

Fig. 13. Top: the undersampled acquisitions shown on a sample slice from the aorta volume. Bottom left: the non-regularized reconstruction. Bottom right: the regularized reconstruction with $\lambda = 5$ and $\alpha = 2$.

volume would have required an acquisition time of 52 s instead of a total acquisition time of 26 s for the two complementary volumes.

Fig. 13-top presents a sample slice extracted from the volume of the aorta (slices are chosen orthogonally to the constant resolution direction, yielding frontal slices). It shows the corresponding slices of the two undersampled volumes, before interpolation; it is easy to visually notice the strong anisotropy of the pixels. Fig. 13-bottom left shows the non-regularized reconstruction ($\lambda = 0$): the resulting volume is corrupted by noise due in part to the oscillations implied by the interpolation of the low-resolution volumes (see Appendix A). Fig. 13-bottom right shows the result with $\lambda = 5$ and $\alpha = 2$ (chosen within the optimal area): noise has been attenuated while edges have been preserved.

Since most clinicians are used to make their diagnosis on maximum intensity projections (MIP) images, we computed the MIPs from the undersampled volumes and from the reconstructed volume; in Fig. 14 we present the projection that best shows the aortic arch.

The results were judged by an expert to be satisfying since they give an accurate anatomic display of the ascending aorta and of the supra-aortic vessels. Such results, allowing a good visualization of vessel walls according to the clinician analysis, have been obtained for the other patients.

6.2. Carotid artery example

For imaging of the carotid arteries an elliptic MRA sequence was used (parameters $T_R = 7.3$ ms and $T_E = 1.6$ ms). The resolutions of the original volumes were $0.59 \times 1.56 \times 1.4$ mm^3, $1.56 \times 1.2 \times 0.59$ mm^3 and $1.2 \times 0.59 \times 1.56$ mm^3, allowing to recover a final volume with voxel size $0.59 \times 0.59 \times 0.59$ mm^3. The duration of each acquisition was 55 s.

As for the aorta, the acquisitions are presented in Fig. 15-top, while the non-regularized reconstruction is shown in Fig. 15-bottom left and the regularized reconstruction is presented in Fig. 15-bottom right (with $\lambda = 5$ and $\alpha = 2$). Fig. 16 presents the MIPs obtained from the same volume, before and after reconstruction without and with regularization. Note that, unlike in Figs. 13 and 14, the displayed acquisitions are already interpolated (by zero-padding).

Again, the expert judged the results to be promising since they allow a high resolution visualization of the vessels and vessel edges.

7. Conclusion

We have presented an accurate modelling of the undersampling in MR imaging systems, and implemented it into an edge-preserving regularized reconstruction method for recovering a high-resolution image from two or three undersampled acquisitions. Using three acquisitions instead of two may be more robust due to the higher redundancy of low-frequency information, but in order to preserve an interesting time gain it is necessary to increase the anisotropy ratio in comparison to the two-acquisition case. Concerning the undersampling ratio, in the two-acquisition case we suggest to use a factor between 3 and 4; in the three-acquisition case, if the resolution is degraded along one direction in each acquisition, a time gain can be achieved for ratios larger than 3, therefore we suggest ratios around 4. If each acquisition is undersampled in the two phase encoding directions, we suggest to use ratios around 2 since a time gain is achieved for ratios starting from $\sqrt{3}$ [27].

Two algorithms have been proposed, based on conjugate gradient and on half-quadratic regularization respectively. Except for a few marginal cases, we have shown that LEGEND has a number of advantages over

Fig. 14. Left and middle: the MIPs computed from both undersampled volumes. Right: the MIP computed after regularized reconstruction with $\lambda = 5$ and $\alpha = 2$.

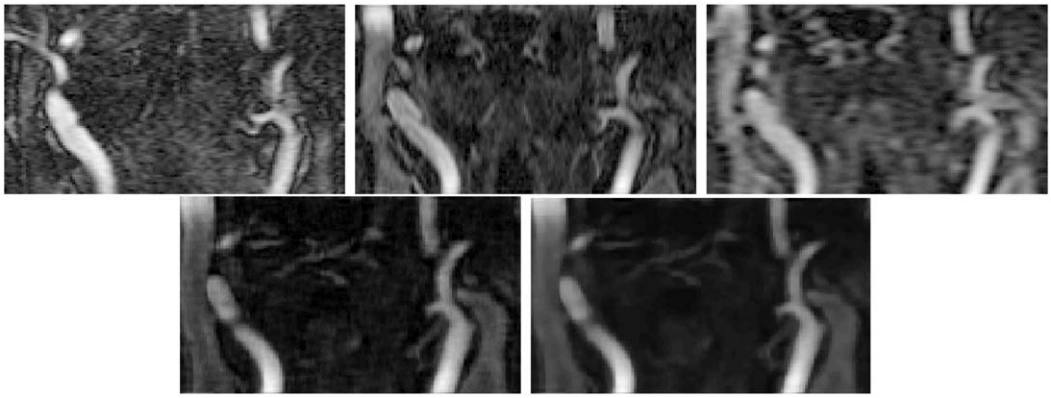

Fig. 15. Top: the undersampled acquisitions shown on a sample slice from the carotids volume. Bottom left: the non-regularized reconstruction. Bottom right: the regularized reconstruction with $\lambda = 5$ and $\alpha = 2$.

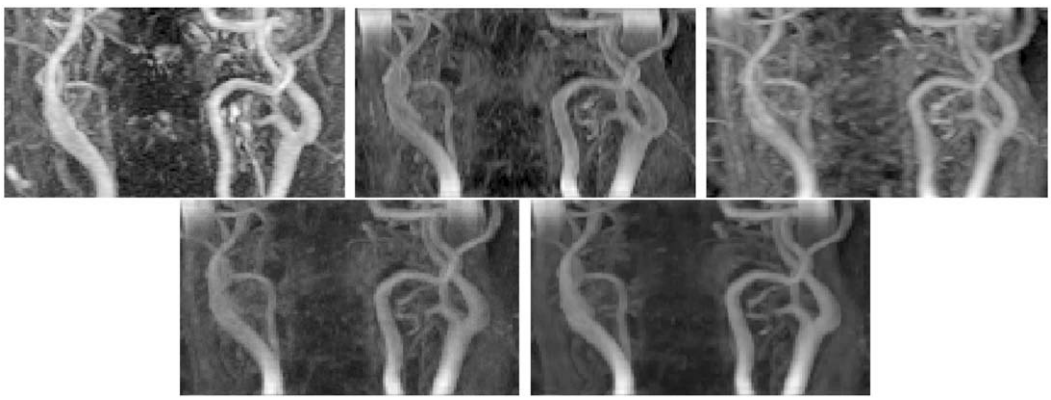

Fig. 16. Top: the undersampled acquisitions shown as a MIP from the neck. Bottom left: the non-regularized reconstruction. Bottom right: the regularized reconstruction with $\lambda = 5$ and $\alpha = 2$.

the conjugate gradient method: it is easier to implement thanks to our formulation in the spectral domain; it shows a better convergence in terms of computation time; it progressively introduces discontinuities. Intensive use of FFTs in the optimization schemes makes the method well designed for Cartesian k-space

filling. However it can be applied to any non-Cartesian acquisition sequence provided that a re-gridding of the data onto a cartesian grid was made previously. It could also be extended to processing data in the genuine non-Cartesian geometry of acquisition. However the FFT computation should then be replaced by a DFT algorithm that would considerably increase the reconstruction time.

We have presented reconstruction results on the aorta, using two acquisitions undersampled in one phase encoding direction, and on the carotid artery, using three acquisitions undersampled in the two phase encoding directions. The reconstruction provides a denoised and homogeneous image of the vascular lumen with sharp edges. Furthermore, although a misalignment of the vessel with respect to the k-space axes can lead to a loss of high frequencies in the acquired data, the method seems to be robust enough to allow any orientations of the vessel. However, for clinical evaluation some further work remains: in this paper, each sequence is acquired in a distinct apnea, which can lead to artifacts due to the breathing of the patient between the acquisitions. A rigid registration was performed manually, which is of course not optimal. Work is currently being performed on the development of dedicated sequences, allowing to acquire the volumes during one breath-holding.

Appendix A. Expression of the zero-padding interpolation

In order not to modify the frequency content of the undersampled data, interpolation is achieved using a special version of the zero-padding method [28]. According to the acquisition strategy presented in Section 2.1, each undersampled image needs to be interpolated in two directions, but this can be achieved separately along both directions. This interpolation is presented here in the x direction as an example.

Let $I_x^{N'}$ be the undersampled image along direction x, with dimension N' along x; let I_x^N be the corresponding high-resolution image, with dimension $N > N'$ along x. (In order to simplify the notations, we assume that both N and N' are even; for odd dimensions, the expressions can be derived by taking the appropriate summation limits.)

Let $J^{N'}$ denote the DFT on the lines of $I_x^{N'}$, and J^N the DFT on the lines of I_x^N. Let us express I_x^N as a function of $I_x^{N'}$.

The expression of $I_x^N(x, y)$ as a function of $J^N(k, y)$ results from an inverse DFT:

$$I_x^N(x,y,z) = \sum_{k=-\frac{N}{2}}^{\frac{N}{2}-1} J^N(k,y,z)\mathrm{e}^{\mathrm{j}2\pi xk/N}. \tag{A.1}$$

Zero-padding interpolation consists in padding the DFT of the signal to be interpolated with zeros in order to artificially increase its spatial sampling rate. Thus, J^N and $J^{N'}$ are related as follows:

$$J^N(k,y,z) = \begin{cases} J^{N'}(k,y,z) & \text{for } k = -\frac{N'}{2} \cdots \frac{N'}{2} - 1 \\ 0 & \text{for } k = -\frac{N}{2} \cdots -\frac{N'}{2} - 1 \\ & \quad \text{and } k = \frac{N'}{2} \cdots \frac{N}{2} - 1. \end{cases} \tag{A.2}$$

Therefore

$$I_x^N(x,y,z) = \sum_{k=-\frac{N'}{2}}^{\frac{N'}{2}-1} J^{N'}(k,y,z)\mathrm{e}^{\mathrm{j}2\pi xk/N}. \tag{A.3}$$

Moreover

$$J^{N'}(k,y,z) = \frac{1}{N'} \sum_{l=-\frac{N'}{2}}^{\frac{N'}{2}-1} I_x^{N'}(l,y,z)\mathrm{e}^{-\mathrm{j}2\pi kl/N'}. \tag{A.4}$$

which yields

$$I_x^N(x,y,z) = \frac{1}{N'} \sum_{l=-\frac{N'}{2}}^{\frac{N'}{2}-1} I_x^{N'}(l,y,z) \times \sum_{k=-\frac{N'}{2}}^{\frac{N'}{2}-1} \mathrm{e}^{-\mathrm{j}2\pi kl/N'}\,\mathrm{e}^{\mathrm{j}2\pi xk/N}. \tag{A.5}$$

Let us introduce $h(m)$ such that

$$I_x^N(x,y,z) = \sum_{l=-\frac{N'}{2}}^{\frac{N'}{2}-1} I_x^{N'}(l,y,z)h\left(x\frac{N'}{N} - l\right). \tag{A.6}$$

$h(m)$ can be expressed as

$$h(m) = \frac{1}{N'} \, \mathrm{e}^{-\mathrm{j}\pi m/N'} \, \frac{\sin \pi m}{\sin(\pi m/N')}, \tag{A.7}$$

The main problem of this conventional zero-padding interpolation method resides in the fact that interpolation of real data provides complex data (for even dimensions). Because of the hypothesis that we are dealing with the magnitude of the M.R. image, i.e. with a real-valued image, it is more convenient to constrain the interpolated image to be real-valued. The solution that minimizes the norm of the quadratic error with respect to the above solution, under the constraint that $h(m)$ must be real-valued, can be computed easily [13,27] as the real part of the above solution, i.e.:

$$h(m) = \frac{1}{N'} \cos\left(\pi \, \frac{m}{N'}\right) \frac{\sin \pi m}{\sin(\pi m/N')}, \tag{A.8}$$

This function is quite similar to the well-known sinc function.

Appendix B. Analytic expression of the undersampling operators

In Section 3.1 the degradation operator was expressed as the matrix product:

$$D_x = F_x^{-1} M_x F_x. \tag{B.1}$$

Let us express D_x analytically:

$$(M_x F_x)_{m,n} = \sum_{k=-\frac{N_x}{2}}^{\frac{N_x}{2}-1} (M_x)_{m,k} (F_x)_{k,n}$$

$$= \begin{cases} \mathrm{e}^{-\mathrm{j}2\pi mn/N_x} & \text{if } -\frac{N_x'}{2}+1 \\ & \quad \leqslant m \leqslant \frac{N_x'}{2}-1, \\ 0.5\,\mathrm{e}^{-\mathrm{j}2\pi mn/N_x} & \text{if } m = -\frac{N_x'}{2} \text{ or} \\ & \quad m = \frac{N_x'}{2}, \\ 0 & \text{else} \end{cases} \tag{B.2}$$

with m, n varying from $-N_x/2$ to $N_x/2 - 1$; thus

$$\begin{aligned} (D_x)_{m,n} &= (F_x^{-1} M_x F_x)_{m,n} \\ &= \sum_{k=-\frac{N_x}{2}}^{\frac{N_x}{2}-1} (F_x^{-1})_{m,k} (M_x F_x)_{k,n} \\ &= \sum_{k=-\frac{N_x'}{2}+1}^{\frac{N_x'}{2}-1} \mathrm{e}^{\mathrm{j}2\pi k(m-n)/N_x} \\ &\quad + 0.5(\mathrm{e}^{\mathrm{j}2\pi((m-n)/N_x)(-N_x'/2)} \\ &\quad + \mathrm{e}^{\mathrm{j}2\pi((m-n)/N_x)(N_x'/2)}) \\ &= \cos\left(\pi \, \frac{n-m}{N_x}\right) \frac{\sin(\pi(n-m)N_x'/N_x)}{\sin(\pi(n-m)/N_x)}. \end{aligned} \tag{B.3}$$

D_y and D_z can be expressed in a similar manner.

Appendix C. Gradient of the energy function

The gradient of the energy function can be expressed as

$$\nabla E(x,y,z) = \nabla Q(x,y,z) + \lambda \nabla \Psi(x,y,z). \tag{C.1}$$

Each of these terms are detailed below.

From the expression of Q in Section 3.2 it can be derived that

$$\begin{aligned} \nabla \mathbf{Q} = 2(&\mathbf{D}_x^{\mathrm{T}} \mathbf{D}_x \mathbf{I}_{\mathrm{rec}} - \mathbf{D}_x^{\mathrm{T}} \mathbf{I}_x + \mathbf{D}_y^{\mathrm{T}} \mathbf{D}_y \mathbf{I}_{\mathrm{rec}} \\ &- \mathbf{D}_y^{\mathrm{T}} \mathbf{I}_y + \mathbf{D}_z^{\mathrm{T}} \mathbf{D}_z \mathbf{I}_{\mathrm{rec}} - \mathbf{D}_z^{\mathrm{T}} \mathbf{I}_z). \end{aligned} \tag{C.2}$$

For the regularization term Ψ also introduced in Section 3.2, we get

$$\begin{aligned} \nabla \mathbf{\Psi} = &\mathbf{\Delta}_x^{\mathrm{T}} \psi'(\mathbf{\Delta}_x \mathbf{I}_{\mathrm{rec}}) + \mathbf{\Delta}_y^{\mathrm{T}} \psi'(\mathbf{\Delta}_y \mathbf{I}_{\mathrm{rec}}) \\ &+ \mathbf{\Delta}_z^{\mathrm{T}} \psi'(\mathbf{\Delta}_z \mathbf{I}_{\mathrm{rec}}). \end{aligned} \tag{C.3}$$

References

[1] H.C. Andrews, B.R. Hunt, Digital Image Restoration, Prentice-Hall, Englewood Cliffs, NJ, 1977.

[2] G. Aubert, M. Barlaud, L. Blanc-Feraud, P. Charbonnier, A deterministic algorithm for edge-preserving computed imaging using legendre transform, in: Proceedings of the IEEE International Conference on Pattern Recognition (ICPR), Vol. 3, 1994, pp. 188–191.
[3] H. Azhari, O.E. Denisova, A. Montag, E.P. Shapiro, Circular sampling: perspective of a time-saving scanning procedure, Magnetic Resonance Imaging 14 (6) (1996) 625–631.
[4] M. Bertero, P. Boccacci, Introduction to Inverse Problems in Imaging, Institute of Physics Publishing, New York, 1998.
[5] M.J. Black, A. Rangarajan, On the unification of line process, outlier rejection, and robust statistics with applications in early vision, Internat. J. Comput. Vision 19 (1) (1996) 57–91.
[6] A. Blake, A. Zisserman, Visual Reconstruction, MIT Press, Cambridge, MA, 1987.
[7] Y. Cao, D.N. Levin, Using prior knowledge of human anatomy to constrain MR image acquisition and reconstruction: half K-space and full K-space techniques, Magnetic Resonance Imaging 15 (6) (1997) 669–677.
[8] P. Charbonnier, L. Blanc-Feraud, G. Aubert, M. Barlaud, Two deterministic half-quadratic regularization algorithms for computed imaging, in: Proceedings of the IEEE International Conference on Image Processing (ICIP), Vol. 2, 1994, pp. 168–172.
[9] P. Charbonnier, L. Blanc-Fraud, G. Aubert, M. Barlaud, Deterministic edge-preserving regularization in computer imaging, IEEE Trans. Image Processing 6 (2) (February 1997) 298–311.
[10] G. Demoment, Image reconstruction and restoration: overview of common estimation structures and problems, IEEE Trans. Acoust. Speech Signal Process. 37 (12) (December 1989) 2024–2036.
[11] E.H. Dillon, M.S. Van Leeuwen, M.A. Fernandez, W.P. Mali, Spiral CT angiography, AJR Amer. J. Roentgenol. 160 (6) (1993) 1273–1278.
[12] I. Dologlou, D. van Ormondt, G. Carayannis, MRI scan time reduction through non-uniform sampling and SVD-based estimation, Signal Processing 55 (1996) 207–219.
[13] D. Fraser, Interpolation by the FFT revisited—an experimental investigation, IEEE Trans. Acoust. Speech Signal Process. 37 (5) (May 1989) 665–675.
[14] D. Geman, C. Reynolds, Non linear image recovery with half-quadratic regularization, IEEE Trans. Image Process. 4 (7) (July 1995) 932–946.
[15] D. Geman, G. Reynolds, Constrained restoration and the recovery of discontinuities, IEEE Trans. Pattern Anal. Machine Intell. 14 (3) (March 1992) 367–383.
[16] S. Geman, D. McClure, Statistical methods for tomographic image reconstruction, Bull. Internat. Statist. Inst. LII-4:5–21 (1987).
[17] T. Hebert, R. Leahy, A generalized EM algorithm for 3-D Bayesian reconstruction from poisson data using Gibbs priors, IEEE Trans. Med. Imaging 8 (2) (June 1989) 194–202.
[18] A. Herment, E. Roullot, I. Bloch, O. Jolivet, A. De Cesare, F. Frouin, J. Bittoun, Local reconstruction of stenosed sections of artery using multiple MRA acquisitions, Magnetic Resonance Med. 49 (2003) 731–742.
[19] R.L. Lagendijk, Iterative identification and restoration of images, Ph.D. Thesis, Technische Universiteit Delft, The Netherlands, 1990.
[20] M. Nikolova, Local strong homogeneity of a regularized estimator, SIAM J. Appl. Math. 61 (2) (1999) 633–658.
[21] D.C. Noll, Multishot rosette trajectories for spectrally selective MR imaging, IEEE Trans. Med. Imaging 16 (4) (August 1997) 372.
[22] J.A. Parker, R.V. Kenyon, D.E. Troxel, Comparison of interpolating methods for image resampling, IEEE Trans. Med. Imaging 2 (1) (March 1983) 31–39.
[23] J.G. Pipe, Motion correction with PROPELLER MRI: application to head motion and free-beating cardiac imaging, Magnetic Resonance Med. 42 (5) (1999) 963–969.
[24] S.K. Plevritis, A. Macovski, MRS imaging using anatomically K-space sampling and extrapolation, Magnetic Resonance Med. 34 (1995) 686–693.
[25] W.K. Pratt, Digital Image Processing, Wiley-Interscience, New York, 1991.
[26] M.R. Prince, Contrast-enhanced MR angiography: theory and optimization, Magnetic Resonance Imaging Clin. N. Amer. 6 (2) (May 1998) 257–267.
[27] E. Roullot, Analysis of multiple anisotropic acquisitions in 3D Magnetic Resonance Angiography: modeling and regularized reconstruction for improving the spatial resolution. Ph.D. Thesis, Ecole Nationale Superieure des Telecommunications, December 2001, (in French).
[28] R.W. Schafer, B. Gold, A digital signal processing approach to interpolation, Proc. IEEE 61 (1973) 692–702.
[29] H. Schomberg, J. Timmer, The gridding method for image reconstruction by Fourier transformation, IEEE Trans. Med. Imaging 14 (3) (September 1995) 596–607.
[30] X. Zhou, Z.P. Liang, S.L. Gewalt, G.P. Cofer, P.C. Lauterbur, A fast echo technique with circular sampling, Magnetic Resonance Med. 39 (1998) 23–27.